Catalysis Today 155 (2010) 108–115

Contents lists available at ScienceDirect

Catalysis Today

journal homepage: www.elsevier.com/locate/cattod

Experimental and numerical investigation of a propane-fueled, catalytic mesoscale combustor

Symeon Karagiannidis [a], Kimon Marketos [a], John Mantzaras [a,*], Rolf Schaeren [a], Konstantinos Boulouchos [b]

[a] Paul Scherrer Institute, Combustion Research, CH-5232 Villigen-PSI, Switzerland
[b] Swiss Federal Institute of Technology, Laboratory of Aerothermochemistry and Combustion Systems, CH-8092 Zurich, Switzerland

ARTICLE INFO

Article history:
Available online 26 May 2010

Keywords:
Mesoscale catalytic combustor
High-pressure propane catalytic reaction rate
Platinum catalyst
Continuum monolith model

ABSTRACT

Small-scale thermochemical devices driven by hydrocarbon-fueled combustors have attracted increased attention for portable power generation applications due to their superior power density compared to state of the art Li-ion batteries. A combined experimental and numerical investigation is presented for the performance characteristics of a mesoscale, propane-fueled, catalytic combustor, to be used in an integrated, gas-turbine-based, mesoscale (ca. 100W_{el}) power generation system. Experiments in an optically accessible reactor led to a global reaction rate for the total oxidation of propane on platinum, valid over the pressure range 1 bar $\leq p \leq$ 7 bar. Parametric numerical studies were subsequently carried out in a single catalytic channel, using a 2D elliptic code with the aforementioned validated kinetic scheme and all relevant heat transfer mechanisms. The predictions identified favorable materials and operating conditions for the burner under consideration. A subscale monolithic honeycomb reactor was finally constructed, based on the findings of the parametric study. The reactor met the set goals for power output as a function of mass throughput. However, heat losses to the environment were responsible for measuring reduced combustor efficiency at certain operating conditions. A continuum model for the entire monolithic structure complemented the experiments and provided the 2D temperature field. Computed exhaust gas temperatures of the monolith were in good agreement with the measurements.

1. Introduction

In recent years, there has been an increased interest towards the production of micro/mesoscale power devices for portable applications [1], with research efforts aiming at providing an alternative to the relatively low power density standard Li-ion batteries. A common approach in many such attempts is the use of hydrocarbon fuels, due to their high energy content that renders even a relatively inefficient device capable of delivering high energy densities [2]. An option for utilizing the chemical energy of hydrocarbons is via a portable micro-compressor/turbine/generator arrangement [3]. As the scale of the device is reduced, however, the resulting increase in surface-to-volume (S/V) ratio gives rise to increased heat losses and radical quenching on the reactor walls. Catalytic combustion is a plausible solution to overcome such issues [4], since it satisfies the requirements of large S/V ratios and moderate operational temperatures relevant to micro/mesoscale devices.

Propane is a fuel of particular interest for micro-energy conversion systems since it liquefies at room temperature and moderate pressures, and is commercially available in compact containers for numerous consumer applications. The study of its complete oxidation over catalytic surfaces constitutes a natural first step towards understanding the similar behavior of higher hydrocarbons. Some of the physical characteristics of propane are common among higher hydrocarbons, such as the larger-than-unity Lewis number (in fuel-lean mixtures with air, the Lewis number of propane is $Le \approx 1.8$), a property directly impacting the surface temperatures [5,6] and the catalytic fuel conversion rate.

The present work undertakes a combined experimental and numerical investigation of a propane-fueled, platinum-coated, mesoscale combustor, which is candidate for portable power generation applications. As a first step, the heterogeneous reactivity of propane on platinum has been assessed with gas-phase Raman spectroscopy, and an appropriate global reaction step for lean propane/air combustion was constructed, valid at pressures 1 bar $\leq p \leq$ 7 bar, a range of interest to microreactors and small-scale industrial turbines. In a second step, a detailed numerical parametric study in a single catalytic channel has been performed, with inlet conditions and combustor material properties as the param-

* Corresponding author. Tel.: +41 56 3104046; fax: +41 56 3102199.
E-mail address: ioannis.mantzaras@psi.ch (J. Mantzaras).

0920-5861/$ – see front matter © 2010 Elsevier B.V. All rights reserved.
doi:10.1016/j.cattod.2010.04.030

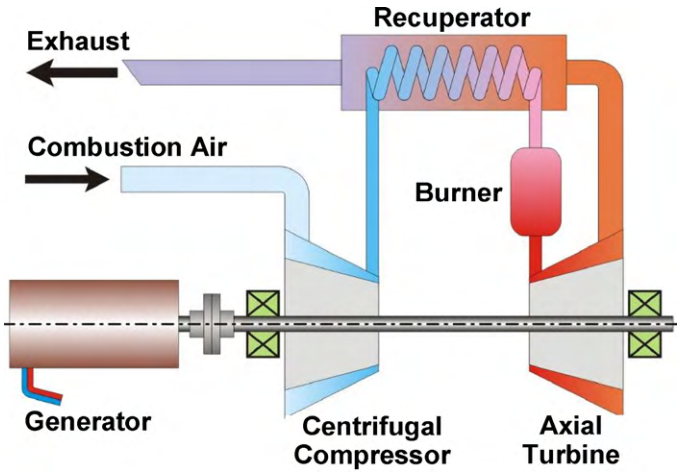

Fig. 1. Mesoscale gas-turbine-based power generator concept [3].

eters of main interest, aimed at defining regimes of optimal power output and fuel conversion. Detailed numerical treatment was provided for the heat transfer mechanisms inside the channel, which included heat conduction in the solid and surface radiation heat exchange between the reactor elements themselves and between the reactor and its surroundings. Based on the findings of the aforementioned parametric study, the third and final step involved the construction and testing of a mesoscale catalytic combustor for a range of operational parameters relevant to micro- and mesoscale power generation applications. A continuum model for the entire combustor monolith was developed to complement the experiments, thus allowing for the simulation of the temperature 2D distribution inside the combustor. This numerical tool facilitated the detailed modeling of the heat losses from the catalytic combustor, evident in the experiments, and allowed for further design improvements.

2. Motivation and background

The pursuit of a mesoscale catalytic combustor was motivated by the initiative to construct a small gas-turbine-driven power generation unit in the order of a few hundred W_{el} (electric) [3]. A demonstration unit is developed for this purpose, with the catalytic combustor specifications dictating a power output of $P_{OUT} = 9400 W_{th}$, a mass flow rate of $m_{IN} = 19.5$ gr/s, an estimated combustor volume of ~200 cm^3 and a corresponding gas hourly space velocity (GHSV) in the order of $10^5\ h^{-1}$. The thermal cycle analysis of the mesoscale gas-turbine unit also dictated a turbine inlet temperature and a target pressure ratio at the compressor discharge of ~1150 K and 2.80, respectively. Catalytic combustion at the mesoscale offers the benefits discussed in the foregoing section, along with simplified combustor design and manufacturing. Moreover, due to the inherent constraints of small-scale turbines (e.g. inability to cool the turbine blades), the use of a catalytic monolithic reactor is particularly advantageous as it allows for relatively low outlet temperatures and low pressure drops. Scaling of such a combustor is simplified by the fact that, once a single channel of the monolith is studied, power output can be adjusted by evaluating the total number of channels required in the monolithic structure. A schematic of the complete power unit system proposed in [3] is depicted in Fig. 1. An overall system efficiency of ~10% is considered, the rule of thumb being that the combustor should have a thermal power roughly ten times the desired electrical power. In order to realize the mesoscale gas-turbine unit, a number of different approaches have been investigated, with the single-stage, recuperated thermal cycle concept chosen not only for ease of design and manufacturing, but also for simplification in the subsequent numerical modeling of the individual components.

3. Experimental

3.1. High pressure test rig

The test rig employed in this study consisted of a high-pressure cylindrical steel vessel with a length of 1.8 m and an internal diameter of 0.28 m (Fig. 2). Visual inspection and optical accessibility of the reactor assembly was achieved via a 50 mm diameter quartz window at the rear flange of the vessel (Fig. 2) and two 350 mm long and 50 mm high quartz windows at the vessel sides (not shown in Fig. 2). Experiments were performed in two different reactors. The first reactor was an optically accessible, channel-flow reactor; therein, the use of *in situ* laser diagnostics allowed for the assessment of the catalytic reactivity of propane on platinum (details of this reactor have been provided elsewhere [7]); the second reactor was a honeycomb subscale unit of the desired catalytic combustor (see Fig. 2), and was used for the evaluation of performance characteristics.

3.2. Optically accessible reactor

The optically accessible, channel-flow catalytic reactor was mounted inside the high-pressure cylindrical vessel and comprised of two horizontal Si[SiC] plates with a length (x) of 300 mm, width (z) of 110 mm and thickness of 9 mm; the plates were positioned 7 mm apart (y) (see [7]). Two 3-mm-thick vertical quartz windows formed the other two reactor sides. The inner surfaces of the Si[SiC] plates were coated via plasma vapor deposition with a 1.5 μm thick Al_2O_3 non-porous layer, followed by a 2.2 μm thick platinum layer. The surface temperatures along the x–y symmetry plane were monitored with S-type thermocouples (12 for each plate). A compressor provided dry air, which was preheated and mixed with propane (grade 3.5 purity) in two sequential static mixers. The preheated propane/air mixture was driven into the reactor through a 50-mm long inert rectangular honeycomb section that provided a uniform inlet velocity profile.

A laser setup employing spontaneous Raman spectroscopy was used to acquire transverse profiles (over the entire 7 mm channel gap) for the major gaseous combustion species C_3H_8, H_2O, N_2, O_2 and CO_2 at different streamwise positions along the channel reactor. The particularly low volumetric content of fuel in lean propane/air combustion necessitated the use of a dedicated high-power laser for the Raman measurements and of propane/air/oxygen mixtures with nitrogen dilution down to 55%, in order to increase the collected signal-to-noise ratio. The 526.5 nm radiation of a frequency-doubled Nd:YLF high repetition rate pulsed laser (Quantronix Darwin Duo), provided the light source for the Raman measurements. Detailed description of the Raman setup and the data analysis have been presented in [8].

3.3. Subscale catalytic combustor

The honeycomb catalytic combustor tested in this work was a subscale version of the desired catalytic combustor for the power unit of Fig. 1, and was embedded inside the high-pressure vessel described in Section 3.2 (see Fig. 2). The reactor comprised a 35 mm inner-diameter, 75 mm long and 1.5 mm thick steel tube, wherein alternating flat and corrugated FeCr-alloy foils (with thickness $\delta = 50$ μm) were rolled-up forming a honeycomb structure with a channel density of 400 cpsi. Visual inspection of the subscale unit revealed an overall good cross-section uniformity for the catalytic channels (see Fig. 2). The unit tested in this study differed from the proposed mesoscale catalytic combustor only in its inner

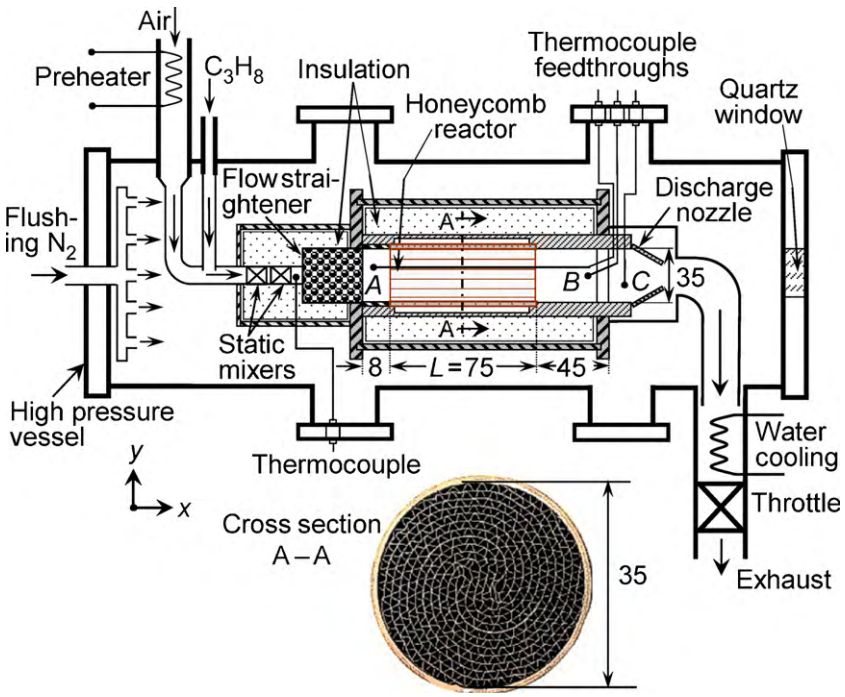

Fig. 2. High-pressure test rig fitted with the honeycomb catalytic combustor. Points A, B and C denote the thermocouple positions. Cross-section A – A presents a top-down view of the subscale catalytic combustor. All distances are in mm.

diameter (all other geometric parameters were kept constant), with the former unit having a radial dimension ~42% smaller than the latter. With the number of catalyst-coated channels being proportional to the honeycomb cross-sectional area, the power output of the subscale unit was reduced nearly three-fold compared to the mesoscale unit; heat losses from the outer combustor surface were accordingly impacted due to the reduced surface area of the subscale combustor. The cross section of each channel was triangular with rounded corners and the equivalent hydraulic radius was $r_h = 0.51$ mm. The FeCr alloy foils were coated with a porous 5%-wt Pt/Al_2O_3 washcoat of ~25 μm thickness. Details on a similar catalyst/washcoat preparation procedure can be found elsewhere [9]. BET and H_2-chemisorption measurements of the fresh Pt-coated foils determined the active-to-geometrical surface ratio of the catalytic washcoat; this value was $B = 12$ and was an input in the continuum model of Section 4.2.

High pressure bottles supplied technical grade (99.5% purity) propane, and dry air was provided by a compressor. Two Brooks mass-flow meters regulated the corresponding flows. The air flow was preheated by a 3 kW resistive heater and then mixed with room temperature propane in two sequential static mixers. A follow-up 40 mm long packing of 2 mm in diameter ceramic spheres straightened the flow. The reactor was mounted inside an insulated (using a 30-mm-thick fiber ceramic material) cylindrical steel frame and was affixed 8 mm downstream of the flow straightener (Fig. 2). Only the first and last 2 mm of the reactor contacted the steel frame, while in the remaining length a 1-mm-thick annular air-cushion was available. In order to regulate the temperature inside the high-pressure vessel, air flowed in the free volume between the reactor and the vessel. The inlet and outlet reactor temperatures were monitored with three 50-μm thick K-type (Ni/Cr–Ni/Al) sheathed thermocouples (designated A, B and C in Fig. 2). The thermocouple beads were positioned at $x = -15$, 95 and 125 mm, with $x = 0$ denoting the beginning of the catalytic section. The absolute accuracy of the gas temperature measurements was ~10 K for the hot outlet and ~6 K for the inlet.

4. Numerical

4.1. Single channel parametric simulations

A full-elliptic 2D CFD code [10,11] was used to simulate a plane channel-flow configuration, which provided the numerical platform for the parametric studies. The channel had a length $L = 75$ mm, height $2b = 1$ mm and wall thicknesses $\delta = 0.1$ mm. All flow conditions were laminar. For the heat conduction in the solid material, a 2-D approach was also adopted with the solid thermal conductivity being either $k = 2$ or 14 W/mK. The outer channel wall surfaces were treated as adiabatic, thus resembling an inner channel of the catalytic monolithic combustor. Parametric studies were carried out by varying the inlet velocity U_{IN} and the fuel-to-air equivalence ratio φ. The inlet pressure was fixed at $p_{IN} = 2.5$ bar, while the inlet mixture preheat was $T_{IN} = 750$ K, considering recuperated operation.

Radiation heat transfer exchange between the discretized catalytic surface elements as well as radiation losses from each internal surface element to the reactor inlet and outlet areas were accounted for by the net radiation method for diffuse-gray areas [12,13]. The inlet, outlet and channel element emissivities were all equal to $\varepsilon = 0.6$. Gas radiative emission and absorption was neglected given the small optical paths and the large nitrogen dilution in the feed. Radiative boundary conditions were applied at the inlet and outlet vertical wall faces, allowing for heat losses towards the surroundings.

Gas-phase chemistry has been shown to affect combustion characteristics in catalytic reactors, even at sub-quenching channel confinements and particularly at elevated pressures [7]. To allow for extended parametric studies, gas-phase chemistry has not been considered. In doing so, a conservative estimate of the stable combustion regimes was obtained, since gas-phase chemistry has been shown to extend the stability limits of catalytic combustors [13]. Finally, mixture-average diffusion provided the gas-phase transport model [14].

Table 1
Material properties of the catalytic monolith. (considering FeCr alloy wall and porous Al_2O_3 washcoat properties).

Heat conduction $k_{c,x}$ (axial direction) (W/mK)	1.80
Heat conduction $k_{c,r}$ (axial direction) (W/mK)	0.20
Density ρ_s (kg/m^3)	1253
Heat capacity c_s (J/kg K)	620

An orthogonal staggered mesh of 24×200 points (in the y- and x-direction, respectively) over half the gas-phase domain with finer spacing near the catalytic walls yielded a grid-independent solution. Two-dimensional solid heat conduction was solved on a uniform grid of 20×200 points. Uniform inlet properties were used for temperature, axial velocity and species mass fractions. No-slip was applied for both velocity components at the gas–wall interface ($y = b$) and zero-Neumann conditions were set at the outlet ($x = L$) and the plane of symmetry ($y = 0$) for the axial velocity and for all thermoscalars.

4.2. Monolith continuum model

In the continuum model approach, the two-dimensional transient energy equation under the finite volume approach for the entire monolithic structure was solved:

$$\frac{\partial(\rho_s c_s T)}{\partial t} = \nabla \cdot (k_c \nabla T) + q, \quad (1)$$

where ρ_s, c_s and k_c are the effective density, heat capacity and thermal conductivity of the solid material, respectively. Table 1 provides the values used in this work, calculated using the properties of the combustor foils and the catalytic washcoat. Variable thermal conductivity in the axial and radial directions was also accounted for [15]. The subscale reactor used in the experiments (Fig. 2) was modeled with a length of $L = 75$ mm and a radius or $R = 17.5$ mm, using a uniform grid of 200×35 point in x and r, respectively. The coupling to the reactive flow fields of the catalytic channels in the monolith was achieved with the use of the heat source term q, calculated for a representative number of channels, which accounted for the heat transfer between gas phase and solid by the change in the integral enthalpy flux of the gas [16]:

$$q = -\sigma \left(\frac{\partial \dot{H}_{GAS}}{\partial x} \right) \quad (2)$$

with q in (W/m^3), σ the channel density and $\dot{H}_{GAS}$ the integral enthalpy flux in the gas phase. In this work, the flow fields of 8 equidistant channels along the monolith radius were computed. The entire honeycomb structure had ~650 channels.

By choosing a time step for the solid integration (Eq. (1)) long enough for gas-phase equilibration, the discretized, time-independent set of the boundary layer equations can be solved for the flow field inside the catalytic channels [17] (quasisteady assumption for the gas phase). After each time step, the resulting axial temperature profiles at the radial positions of the 8 selected channels were applied as boundary conditions for the flow field channel calculations. It is noted that even though the time integration of Eq. (1) provided the transient response of the reactor, of interest in this work is only the steady-state solution wherein experimental data were available. Heat losses due to radiation at the monolith inlet and outlet along with convective heat losses from its outer wall surface were included as boundary conditions. In the model, the inlet and outlet enclosures were treated as black bodies with temperatures equal to the inlet and outlet gas temperatures, respectively (values taken directly from the experiments), while the convective heat transfer coefficient (see Fig. 3) was varied to match the experimentally observed exhaust gas temperatures. Surface reaction rates were evaluated with Surface-CHEMKIN [18],

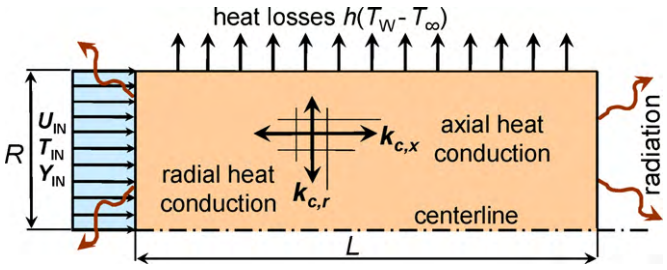

Fig. 3. Schematic of the continuum model for the monolith structure.

while mixture-average diffusion was the transport model, using the CHEMKIN transport database [14].

5. Results and discussion

5.1. Global step catalytic reaction

Recent catalytic combustion studies [7] have shown that the heterogeneous reactivity of hydrocarbons on platinum follows a positive power law pressure dependence, which bears the combined effects of a positive, typically first-order reaction dependence with respect to fuel concentration in the gas phase over the catalyst surface, and a negative dependence due to the reduction of free platinum sites with increasing oxygen partial pressure. The latter mechanism is very important in restraining the rate of increase of the catalytic reactivity with rising pressure. The challenge in a global catalytic step is to reproduce the reactivity over a wide range of operating conditions (pressures and temperatures).

In a fashion similar to earlier methane studies [7], the global step of Garetto et al. [19] for propane oxidation on platinum at atmospheric pressure was extended to higher pressures by introducing a pressure correction term which restrained the rate of increase of the catalytic reactivity with rising pressure [8]:

$$\dot{s}_{C_3H_8} = A \times \left(\frac{p}{p_0} \right)^{-n} \times T_W^{1.15} \times \exp\left(\frac{-E_a}{RT_W} \right) \times [C_3H_8]_W^{\alpha}, \quad (3)$$

with the catalytic rate $\dot{s}_{C_3H_8}$ in (mol/cm^2 s), $A = 93.2\ \mathrm{K}^{-1.15}\ \mathrm{cm}^{1.45}\ \mathrm{mol}^{-0.15}\ \mathrm{s}^{-1}$, $E_a = 71.128$ kJ/mol, $\alpha = 1.15$, the concentration of propane $[C_3H_8]$ in (mol/cm^3), n a positive number smaller than unity and $p_0 = 1$ bar. The subscript w denotes conditions at the gas–wall interface. For a value of $n = 0.4 \pm 0.03$, the extended global step captured well the near-wall bending of the experimentally acquired propane boundary layer profiles, over the pressure range 1 bar $\le p \le$ 7 bar. Fig. 4 provides a comparison between numerically predicted (using the extended global step) and experimentally observed (Raman data) transverse profiles of propane and water mole fractions over the transverse distance of the channel flow reactor at selected axial locations for two pressures. The good agreement between experimental and numerical results evident in Fig. 4 confirms the validity of the pressure-corrected global step for describing lean propane/air combustion on platinum. It is noted that the experiments presented in Fig. 4 have been performed using propane/air (instead of propane/air/oxygen in [8]) mixtures and were used to validate the extended global step under real operating conditions.

5.2. Single channel parametric study

In the ensuing calculations, thermal power outputs were computed and combustion efficiencies were estimated. The wall thermal conductivity was set to $k = 2.0$ or 14 W/mK, thus simulating a ceramic and a metallic reactor (these values roughly correspond to cordierite and FeCr alloy materials, respectively). Mixture compres-

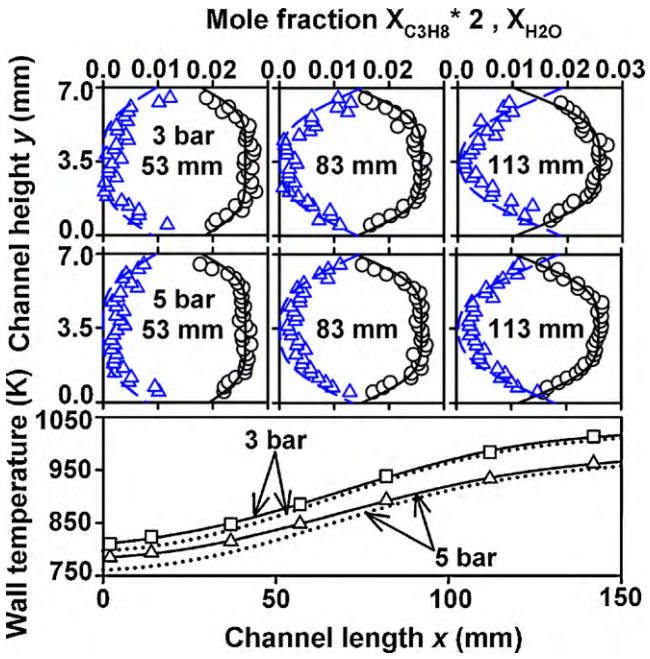

Fig. 4. Measured and predicted transverse profiles of C_3H_8 and H_2O mole fractions at three streamwise locations for T_{IN} = 449 K, φ = 0.31, U_{IN} = 1.61 and 0.96 m/s, at 3 and 5 bar, respectively. Measurements: C_3H_8 (circles), H_2O (triangles). Predictions: C_3H_8, solid lines; H_2O, dashed-dotted lines. Upper- and lower-wall (solid and dotted-lines, respectively) temperature profiles fitted through thermocouple measurements (symbols indicate thermocouple positions).

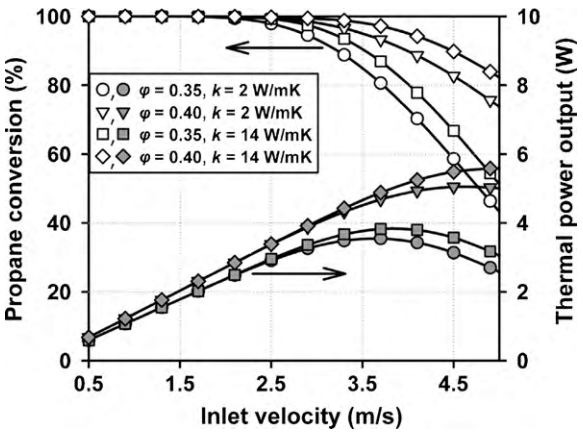

Fig. 6. Fuel conversion (open symbols) and thermal power output (gray symbols) versus inlet velocity. Thermal power output is computed for a channel of 1 mm² cross section.

sion was fixed at p = 2.5 bar, the equivalence ratios were φ = 0.40, 0.35 and 0.33, while the channel wall thickness was δ = 0.1 mm. The forthcoming diagrams were constructed by one-parameter continuation of the mixture inlet velocity U_{IN}, which was increased until a critical value was reached with marked drop in reactor performance. The main objective was to construct power curves for a given reactor geometry, material properties, and inlet conditions. An example of the results obtained can be seen in Fig. 5, where temperature and fuel distributions inside the channel are provided for two cases with equivalence ratio φ = 0.35, thermal conductivity k = 14 W/mK and two inlet velocities U_{IN} = 2.3 and 4.5 m/s. As will become evident later in Fig. 6, both cases exhibited similar thermal

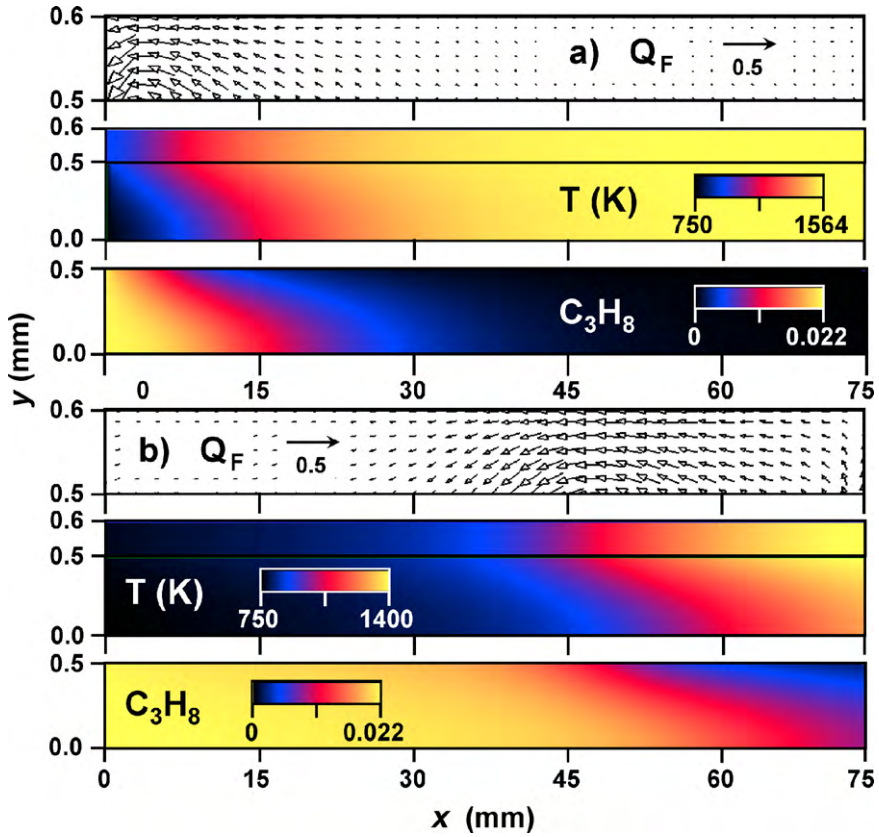

Fig. 5. Two-dimensional distributions of temperature and propane mass fraction and heat flux vector plot in the solid (top, middle and bottom panels, respectively) for two cases with φ = 0.35, k = 14 W/mK and a) U_{IN} = 2.3 m/s, b) U_{IN} = 4.5 m/s. Reference vectors denote heat flux magnitude of 0.5 W/mm². The plane of symmetry is at y = 0 and the gas–solid interface at y = 0.5 mm (color online).

power outputs but differed substantially in overall propane conversion efficiency. The heat flux inside the solid wall is visualized with the help of vector plots. It is clarified that the transverse temperature differences inside the solid were very small (up to 1.5 K over the entire 0.1 mm channel wall thickness).

Thermal power curves and combustion efficiencies for a reactor length $L = 75$ mm and a channel cross-section of 1 mm × 1 mm (1 mm lateral channel dimension) are summarized in Fig. 6. The velocity ranges from $U_{IN} = 0.5$ m/s, the lowest value for all cases studied in this work, to 5.0 m/s; the latter is arbitrarily chosen as a representative value where the combustion efficiency (defined as the temperature rise of the gas at the channel outlet over the potential adiabatic temperature rise) drops significantly.

For moderate inlet velocities, which can reach up to 2.5 m/s for the conditions in Fig. 6, a linear increase in thermal power output is observed with rising inlet velocity. The combustion efficiency remains high since almost complete fuel conversion is achieved (~99.99%), while the power output is directly proportional to the equivalence ratio. As long as fuel conversion is nearly complete, no difference is observed between reactors of different solid thermal conductivities. The linearity in reactor response ceases as the inlet velocity approaches a critical value. With increasing inlet velocity, every power curve reaches a maximum. These maxima lie at combustion efficiencies (i.e. fuel conversions) of 71–83% for all cases considered.

The effect of wall thermal conductivity is more pronounced at high inlet velocities, where increased efficiency is observed in the case of high solid thermal conductivity, as seen in Fig. 7 pertaining to $U_{IN} = 3.7$ m/s. In this graph, axial profiles of the energy heat balance terms in the solid are provided in terms of all modeled heat transfer modes: heat generated via reactions on the surface, heat convected to the gas, heat conducted through the channel wall and net radiation heat exchange. The radiation exchange contribution is altogether minimal and for clarity it has been multiplied by a factor of five. A small amount of heat is conducted inside the solid wall for $k = 14$ W/mK (the corresponding amount for $k = 2$ W/mK is negligible). In the former case, the amount of heat feedback to the reactor front via solid conduction is much smaller compared to the maximum heat generation; nonetheless, this small amount is crucial in reducing the light-off distance and thus increasing the combustion efficiency.

Another interesting observation is presented in Fig. 8. Average gas temperatures at the reactor outlet are plotted versus the inlet

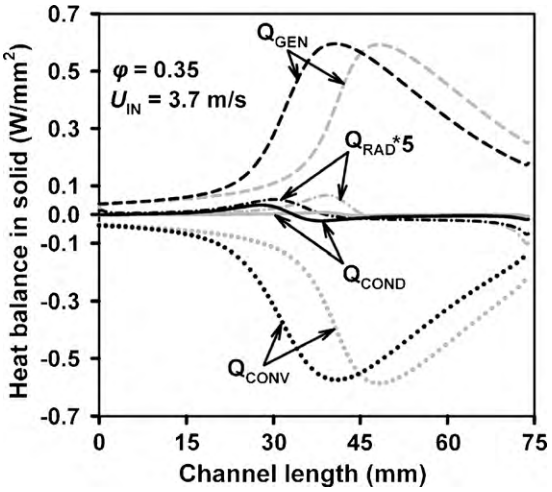

Fig. 7. Axial heat balance in the solid wall for $k = 2$ W/mK (gray curves) and 14 W/mK (black curves). Dashed curves: heat generated from catalytic reactions. Dotted curves: heat convected to the gas. Solid curves: heat conducted in the solid. Dash-dotted curves: net radiation exchange.

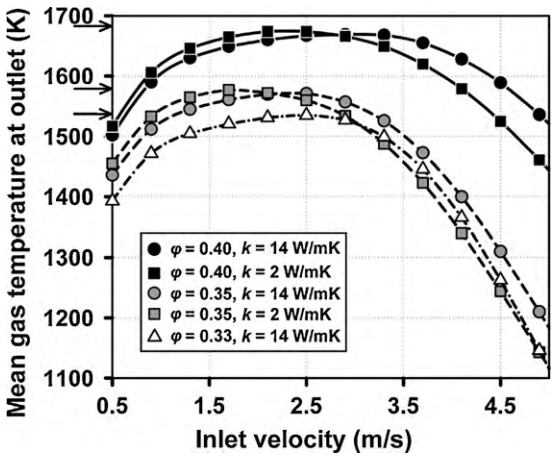

Fig. 8. Mean gas temperature at the channel outlet versus inlet velocity for three equivalence ratios and thermal conductivities k of 2 and 14 W/mK. The horizontal arrows on the y axis denote adiabatic temperatures for $\varphi = 0.33$, 0.35 and 0.40 at $T_{ad} = 1537$, 1579 and 1683 K, respectively.

velocity for the two different solid thermal conductivities and for the equivalence ratios in Fig. 6. For comparison purposes, average gas temperatures are also plotted for $k = 14$ W/mK and $\varphi = 0.33$. At the low inlet velocity regime (up to ~1.5 m/s), although complete fuel conversion is achieved, the outlet gas temperatures deviate significantly from the adiabatic flame temperature for the given inlet conditions of mixture preheat and fuel/air equivalence ratio. Radiation exchange between the cold inlet section and the hot channel walls near the entry is proportional to the fourth power of temperature of these surfaces, while heat generation inside the channel is proportional to the mass inflow. As the equivalence ratio is increased, it becomes less favorable to operate at low inlet velocities, an observation which holds true for both high and low wall thermal conductivities, even though the higher residence times and wall temperatures favor complete fuel conversion. The associated high adiabatic temperature rise necessitates higher inlet velocities to compensate for the higher radiation heat losses.

5.3. Experimental testing of mesoscale combustor

The foregoing parametric study of a single catalytic channel dictated the construction of a mesoscale combustor with metallic walls, operating at high inlet velocities and low equivalence ratios, with the dimensioning mentioned in the experimental section. The combustor was subsequently tested for the experimental conditions of Table 2. For a given set of inlet pressure p_{IN}, equivalence ratio φ and inlet temperature T_{IN}, the mass inflow (air and propane streams) was varied from a minimum of 2.3 gr/s up to 6.6 gr/s with increments of ~0.5 gr/s. After each mass inflow increment, exhaust gas temperature measurements were recorded once the combustor reached steady state. Only heterogeneous combustion was considered and in a fashion similar to earlier studies [20], combustor efficiency was calculated by comparing the average temperature rise over the catalytic reactor $\Delta T = (T_B + T_C)/2$, T_B and T_C being the exhaust gas thermocouple measurements at the combustor outlet, with the potential adiabatic temperature gain $\eta = \Delta T/(T_{ad} - T_{IN})$, with T_{ad} calculated for the corresponding inlet conditions. Total

Table 2
Mesoscale catalytic combustor experimental conditions.

Inlet pressure p_{IN} (bar)	1.2, 2.0, 3.0, 5.0
Inlet temperature T_{IN} (K)	604–750
Equivalence ratio φ	0.20, 0.25, 0.30, 0.33
Mass inflow m_{IN} (gr/s)	up to 6.6

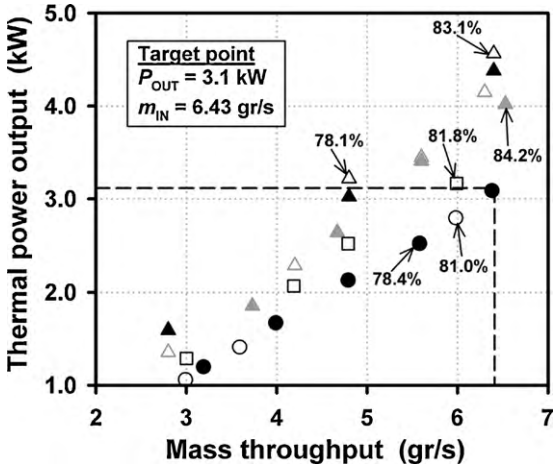

Fig. 9. Combustor thermal power output versus mass throughput deduced from measurements; p_{IN} = 2 and 3 bar (closed and open symbols), T_{IN} = 600 and 700 K (black and gray symbols) and φ = 0.2, 0.25 and 0.3 (circles, squares and triangles, respectively). For selected cases, combustor efficiencies are indicated on the graph. The target point for the subscale combustor was set at P_{OUT} = 3100 W at a mass inflow of m_{IN} = 6.43 gr/s.

thermal power output for the combustor was subsequently calculated based on chemical energy input for the given inlet conditions and propane conversion.

Measured operational maps of thermal power output versus mass inflow, such as the one provided in Fig. 9, were constructed based on efficiency measurements for various sets of inlet pressures, temperatures and mixture compositions. These maps provided validation of the initial combustor design concept, since the target operational point of power output and mass throughput, as dictated by the thermodynamic analysis of the gas-turbine-driven power unit, was met or even exceeded by the combustor at various sets of inlet conditions. Fig. 10 provides power output curves measured for a fixed equivalence ratio and inlet temperature over the entire pressure range investigated. A significant rise in performance is evident as the inlet pressure is increased, with an almost threefold gain in power output for a fivefold increase in inlet pressure, at the maximum mass inflow value tested. It is emphasized that the correct kinetic expression with an appropriate pressure exponent derived in the first part of this study (Eq. (3)) is cardinal in assessing the effect of pressure. A combination of reduced catalytic reactivity and short residence times at the

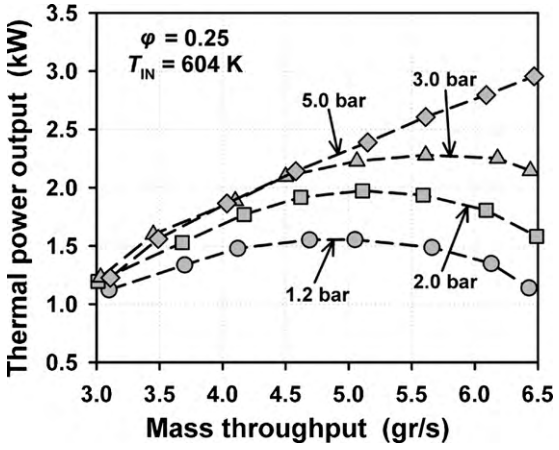

Fig. 10. Thermal power output versus mass throughput, measured for an equivalence ratio φ = 0.25 and inlet temperature T_{IN} = 604 K, over the investigated pressure range 1 bar ≤ p_{IN} ≤ 5 bar.

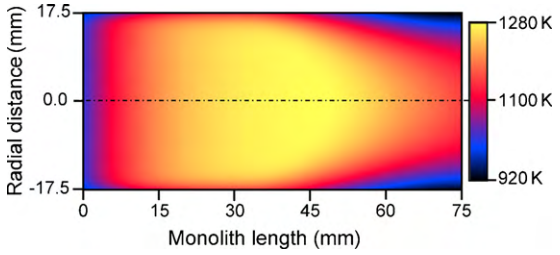

Fig. 11. Computed two-dimensional temperature distribution inside the catalytic monolith. The conditions are: p_{IN} = 3.01 bar, φ = 0.20, inlet temperature T_{IN} = 713 K, inlet velocity U_{IN} = 3.21 m/s, heat losses $h(T_w - T_\infty)$ with h = 12 W/m^2 K and T_∞ = 300 K.

low inlet pressures are, to a certain extent, responsible for the significant efficiency differences between operating pressures at constant mass inflows. However, for all cases considered in this work, the maximum combustor efficiency observed was ~85%, which indicates that heat losses to the surroundings and potential fuel breakthrough can further reduce the thermal power output of the combustor.

5.4. Continuum model simulations

Numerical simulations of the 2D temperature distribution inside the catalytic monolith were performed using the continuum model approach described earlier, in order to facilitate the experiments conducted with the subscale model by providing insight on thermal management issues of the mesoscale combustor (namely radiation losses and heat losses from the outer honeycomb surface). By varying only the external heat losses coefficient at the outer reactor surface, the computed outlet gas temperature of the monolith was matched with the exhaust gas thermocouple measurements at the combustor outlet. In all cases, good agreement within ~5% of the experimental values was achieved.

The 2D temperature field of the monolith is presented for a selected case in Fig. 11, representative of the continuum model simulations. Mean outlet gas temperatures computed for the individual reactor channels allowed for an estimate of the average exhaust gas temperature of the monolith. In the case of Fig. 11, the computed outlet gas temperature was at 1089 K, as opposed to a measured value of 1041 K for the same experimental conditions. This figure also illustrates the strong variation of temperature in the radial direction over the axial length covering the rear half of the reactor. CFD simulations of the single monolith channels for this case revealed that fuel is already consumed up to 99% at half the reactor length, which in turn renders the rest of the reactor volume a heat sink towards the environment. Reduced radial heat transfer (due to the spatially non-uniform thermal properties of the monolith) reduces the amount of external heat losses; however these are large enough to drop the overall combustor efficiency down to 74% for this particular case. It should be noted that the large Lewis number of propane in fuel-lean compositions with air necessitates increased reactor lengths due to the reduced transverse transport of the fuel towards the reactor walls. The correct chemical expression derived from the first part of this work allows tuning the required reactor length with greater accuracy and thus reducing the unused part of the monolith, which serves only as a heat sink to the environment.

6. Conclusions

A propane-fueled, catalytic, mesoscale combustor was investigated numerically and experimentally to assess its applicability for a portable, gas-turbine-based power generation application. An

optically accessible catalytic reactor was employed to establish a correct global step expression for propane combustion on platinum, for pressures up to 7 bar. Detailed parametric studies of a single catalytic channel revealed that, for a given reactor length, metallic materials are more favorable regarding maximum thermal power output and combustion efficiency. Radiation heat losses were more pronounced at the low inlet velocity regime and, moreover, had a greater impact at higher equivalence ratios. A subscale model of the catalytic combustor was constructed and tested under conditions dictated by the requirements of the power generation unit that met the required power output at the nominal mass throughput. Experiments revealed the positive effect of elevated operating pressures on the overall combustion efficiency, while significant heat losses of the monolith to the environment were evident. A continuum model was finally used to simulate the two-dimensional temperature field of the monolith, allowing for detailed description of the heat loss mechanisms. The latter tool, combined with the correct reaction rate expression for propane on platinum established earlier, provided the reactor length needed for full fuel conversion.

References

[1] A.C. Fernandez-Pello, Proc. Combust. Inst. 29 (2002) 883–899.
[2] A. Gomez, J.J. Berry, S. Roychoudhury, B. Coriton, J. Huth, Proc. Combust. Inst. 31 (2007) 3251–3259.
[3] S.K.B. Schneider, M. Bruderer, D. Dyntar, C. Zwyssig, Q. Guangchun, M. Diener, K. Boulouchos, R.S. Abhari, L. Guzzella, J.W. Kolar, Ultra-high-energy-density converter for portable power, in: Power-MEMS 2005, Tokyo, Japan, November 28–30, 2005.
[4] K. Maruta, K. Takeda, J. Ahn, K. Borer, L. Sitzki, P.D. Ronney, O. Deutschmann, Proc. Combust. Inst. 29 (2002) 957–963.
[5] J. Mantzaras, Interplay of transport and hetero-/homogeneous chemistry, in: S.Z. Jiang (Ed.), Focus on Combustion Research, Nova Publishers, New York, 2006, p. 241.
[6] W.C. Pfefferle, L.D. Pfefferle, Prog. Energy Combust. Sci. 12 (1986) 25–41.
[7] M. Reinke, J. Mantzaras, R. Schaeren, R. Bombach, A. Inauen, S. Schenker, Combust. Flame 136 (2004) 217–240.
[8] S. Karagiannidis, J. Mantzaras, R. Bombach, S. Schenker, K. Boulouchos, Proc. Combust. Inst. 32 (2009) 1947–1955.
[9] S. Eriksson, M. Wolf, A. Schneider, J. Mantzaras, F. Raimondi, M. Boutonnet, S. Järas, Catal. Today 117 (2006) 447–453.
[10] M. Reinke, J. Mantzaras, R. Schaeren, R. Bombach, A. Inauen, S. Schenker, Proc. Combust. Inst. 30 (2005) 2519–2527.
[11] C. Appel, J. Mantzaras, R. Schaeren, R. Bombach, A. Inauen, B. Kaeppeli, B. Hemmerling, A. Stampanoni, Combust. Flame 128 (2002) 340–368.
[12] R. Siegel, J.R. Howell, Thermal Radiation Heat Transfer, Hemisphere, New York, 1981, p. 271.
[13] S. Karagiannidis, J. Mantzaras, G. Jackson, K. Boulouchos, Proc. Combust. Inst. 31 (2007) 3309–3317.
[14] R.J. Kee, G. Dixon-Lewis, J. Warnatz, M.E. Coltrin, J.A. Miller, A Fortran computer code package for the evaluation of gas-phase multicomponent transport properties, Report No. SAND86-8246, Sandia National Laboratories, 1996.
[15] G. Groppi, E. Tronconi, AIChE 42 (1996) 2382–2387.
[16] S. Tischer, O. Deutschmann, Catal. Today 105 (2005) 407–413.
[17] K.E. Brenan, S.L. Campbell, L.R. Petzold, Numerical Solution of Initial-Value Problems in Differential-Algebraic Equations, Prentice Hall, New York, 1989.
[18] M.E. Coltrin, R.J. Kee, F.M. Rupley, Surface Chemkin: a Fortran package for analyzing heterogeneous chemical kinetics at the solid surface-gas phase interface, Report No. SAND90-8003C, Sandia National Laboratories, 1996.
[19] T.F. Garetto, E. Rincon, C.R. Apesteguia, Appl. Catal. B: Environ. 48 (2004) 167–174.
[20] R. Carroni, T. Griffin, J. Mantzaras, M. Reinke, Catal. Today 83 (2003) 157–170.